

RSC Advances



This is an *Accepted Manuscript*, which has been through the Royal Society of Chemistry peer review process and has been accepted for publication.

Accepted Manuscripts are published online shortly after acceptance, before technical editing, formatting and proof reading. Using this free service, authors can make their results available to the community, in citable form, before we publish the edited article. This *Accepted Manuscript* will be replaced by the edited, formatted and paginated article as soon as this is available.

You can find more information about *Accepted Manuscripts* in the [Information for Authors](#).

Please note that technical editing may introduce minor changes to the text and/or graphics, which may alter content. The journal's standard [Terms & Conditions](#) and the [Ethical guidelines](#) still apply. In no event shall the Royal Society of Chemistry be held responsible for any errors or omissions in this *Accepted Manuscript* or any consequences arising from the use of any information it contains.

Mass production of $\text{Li}_4\text{Ti}_5\text{O}_{12}$ with conductive network via In-situ spray pyrolysis as a long cycle life, high rate anode material for lithium ion batteries

Guodong Du, Brad R. Winton, Israa M. Hashim, Neeraj Sharma, Konstantin Konstantinov, M. V. Reddy, Zaiping Guo**

Dr. G.D. Du, Dr. B.R. Winton, Ms. I.M. Hashim, Prof. Z.P. Guo, Dr. K. Konstantinov
Institute for Superconducting and Electronic Materials
University of Wollongong, NSW, 2522, Australia
E-mail: zguo@uow.edu.au; konstan@uow.edu.au

Dr. N. Sharma
School of Chemistry, University of New South Wales, Sydney, NSW, 2052, Australia

Prof. Z.P. Guo
School of Mechanical, Materials and Mechatronic Engineering
University of Wollongong, NSW 2522, Australia

Dr. M. V. Reddy
Department of Physics, National University of Singapore, Singapore, 117542

Keywords: $\text{Li}_4\text{Ti}_5\text{O}_{12}$, spray pyrolysis, anode, high rate, lithium ion batteries

Abstract

Nanocrystalline $\text{Li}_4\text{Ti}_5\text{O}_{12}$ with in-situ incorporation of carbon and Ti^{3+} was synthesized by industry scalable in-situ spray pyrolysis, producing crystal sizes ranging from 10 to 30 nm. Subsequent annealing in N_2 preserved a proportion of the carbon from the precursor organic salts, predominantly on the $\text{Li}_4\text{Ti}_5\text{O}_{12}$ grain boundaries, where it formed a conductive network. Such a situation would be expected to inhibit the growth of the primary $\text{Li}_4\text{Ti}_5\text{O}_{12}$ crystals. The molecular-level uniformity of the precursor allows synthesis of $\text{Li}_4\text{Ti}_5\text{O}_{12}$ with a significantly shorter heat treatment compared to conventional solid state reaction, which in turn saves energy during large-scale production. Notably, both the nanosized particles and the

in-situ incorporation of carbon and Ti^{3+} improve the rate capability. In rate capability measurements, stable and high capacity retention was observed from 0.5 C to 30 C. Spray pyrolyzed $\text{Li}_4\text{Ti}_5\text{O}_{12}$ delivered a discharge capacity of 145.8 mAh g^{-1} at 10 C for up to 500 cycles. In the full battery tests with $\text{Li}(\text{Co}_{0.16}\text{Mn}_{1.84})\text{O}_4$ as cathode, it also shows excellent capacity and cycling stability, further indicating that spray pyrolyzed $\text{Li}_4\text{Ti}_5\text{O}_{12}$ is a promising anode material for high power batteries.

Introduction

A drive for renewable clean energy options to be utilized at higher levels exists due to the increasing concerns about the shortage of crude oil and the consequences of global warming. As a result, lithium ion batteries have been recently developed to provide power for electric vehicles (EVs) or hybrid electric vehicles (HEVs) in order to reduce environmental pollution [1-3]. However, the performance of the conventional carbon anode in lithium ion batteries can not meet all the requirements of modern EVs, such as the need for high-rate cycling or fast charging. Moreover, safety issues with the use of commercial carbon are not well addressed, which include its low working voltage and lithium dendritic growth under high current if the battery is overcharged [4]. Therefore, cost-effective anode materials with high power densities that are safe and feature long cycle lives are required.

As an alternative, spinel $\text{Li}_4\text{Ti}_5\text{O}_{12}$ is under serious consideration as an anode in high power cells [5], owing to it having the following advantages: a working potential of 1.5 V vs. Li^+/Li , high thermal stability, especially at elevated temperatures, and

enhanced safety. Since a solid electrolyte interphase (SEI) forms below 1 V vs. Li^+/Li , in part due to the reduction of the organic electrolyte, having a working voltage above 1 V, as in $\text{Li}_4\text{Ti}_5\text{O}_{12}$ anodes, can avoid the SEI formation and may also avoid lithium plating under high current conditions [6]. $\text{Li}_4\text{Ti}_5\text{O}_{12}$ can accommodate three further lithium cations in its structure and shows very flat charge/discharge curves during electrochemical cycling. Moreover, $\text{Li}_4\text{Ti}_5\text{O}_{12}$ is referred to as a “zero strain” material during the transition between the two end members, $\text{Li}_4\text{Ti}_5\text{O}_{12}$ and $\text{Li}_7\text{Ti}_5\text{O}_{12}$, with lithium intercalation/de-intercalation, resulting in stable cycling due to the negligible volume change [7]. However, the low electronic conductivity and moderate Li^+ diffusion coefficient hinder its high rate performance and applicability for Li-ion batteries [8]. The conventional methods to improve rate capability are minimizing the particle size to decrease the Li^+ diffusion length and carbon coating to improve the conductivity [9, 10]. The practical problems imply that it is not easy to prepare $\text{Li}_4\text{Ti}_5\text{O}_{12}$ nanostructures, and it is also difficult to control the uniformity of the carbon coating if extra organic carbon sources are used.

Above all, for industrial application, the laboratory-based synthesis procedure should be low-cost, energy non-intensive, and facile and feasible for scaled up production. Commonly for most titanium salts, the starting precursors are easily hydrolyzed to form TiO_2 . Once TiO_2 is formed, it is necessary to heat it with lithium salts at high temperatures for extended periods of time in order to obtain well-crystallized $\text{Li}_4\text{Ti}_5\text{O}_{12}$, which is an energy consuming process [9]. Furthermore, due to the time-consuming heat treatment at high temperatures, the $\text{Li}_4\text{Ti}_5\text{O}_{12}$ particle

sizes grow to several hundred nanometers or even several microns, which, in turn, increases the lithium diffusion path within isolated particles and thereby decreases electrode performance. Spray pyrolysis is a well-known cost effective and industrially scalable technique, providing the capability to manufacture large numbers of nanostructured ceramics and composites with promising applications in energy storage devices [11]. Precursor salts are dissolved in a solution that allows uniform mixing of each component at the molecular level, leading to high chemical purity in the products. Spray pyrolysis with appropriately chosen precursor salts is expected to save on heat treatment times, and thus save energy and cost in large-scale production.

In the present work, $\text{Li}_4\text{Ti}_5\text{O}_{12}$ was prepared by an in-situ spray pyrolysis technique in the form of nanocrystallites. Both the uniformity of the precursor components and the pre-formed crystallites allowed subsequent short annealing times, which are required to save energy in large-scale production. Meanwhile, the heat treatment under N_2 atmosphere preserves carbon from the decomposed organic precursors, forming in-situ carbon-containing samples, thus improving the conductivity and allowing favorable electrochemical performance.

Results and discussion

Morphologies of raw $\text{Li}_4\text{Ti}_5\text{O}_{12}$ (raw LTO) and of $\text{Li}_4\text{Ti}_5\text{O}_{12}$ annealed in N_2 (LTO-N) and in air (LTO-A) were investigated by transmission electron microscopy (TEM) and are presented in **Figure 1**. All samples show micron-size spheres which are the typical features of materials prepared by the spray pyrolysis technique. The high resolution images of the three samples, are shown as follows: raw LTO (Fig. 1(b)), LTO-N (Fig.

1(d)), and LTO-A (Fig. 1(f)). Raw LTO shows a mesoporous structure with a high specific surface area of $74.5 \text{ m}^2 \text{ g}^{-1}$. The selected area electron diffraction (SAED) pattern of raw LTO shows very diffuse diffraction rings, indicating that the sample was not well crystallized, but is in a semicrystalline and semi-amorphous state, which is consistent with the broad and weak intensities observed in the XRD pattern and the poorly developed fringes in some areas, with crystal sizes of about 5 nm, as shown in the high resolution TEM image in **Figure S1** in the **Supporting Information (S)**. The homogeneous morphology and structure of the raw LTO can be attributed to the mixing of the precursor solution on the atomic level and the ultra-fast spray pyrolysis process (around 0.5 s) in the furnace at 800 °C. Thus, the crystallites are formed but not well developed, and the subsequent evaporation process involving the escape of the solvent results in a mesoporous sample. As for the LTO-N sample, the inset in Figure 1(c) shows bright and sharp diffraction rings, indicating a well crystallized sample. The particles within the polycrystalline sample were of the order of 10 – 30 nm in size, a size range which is difficult to synthesize by conventional solid state reaction, as the long heating times required tend to form micron-size particles. Notably, the LTO-A sample shows non-uniform crystal sizes (Figure 1(f)), with a significant fraction of crystallites around 100 nm and numerous microtwins.

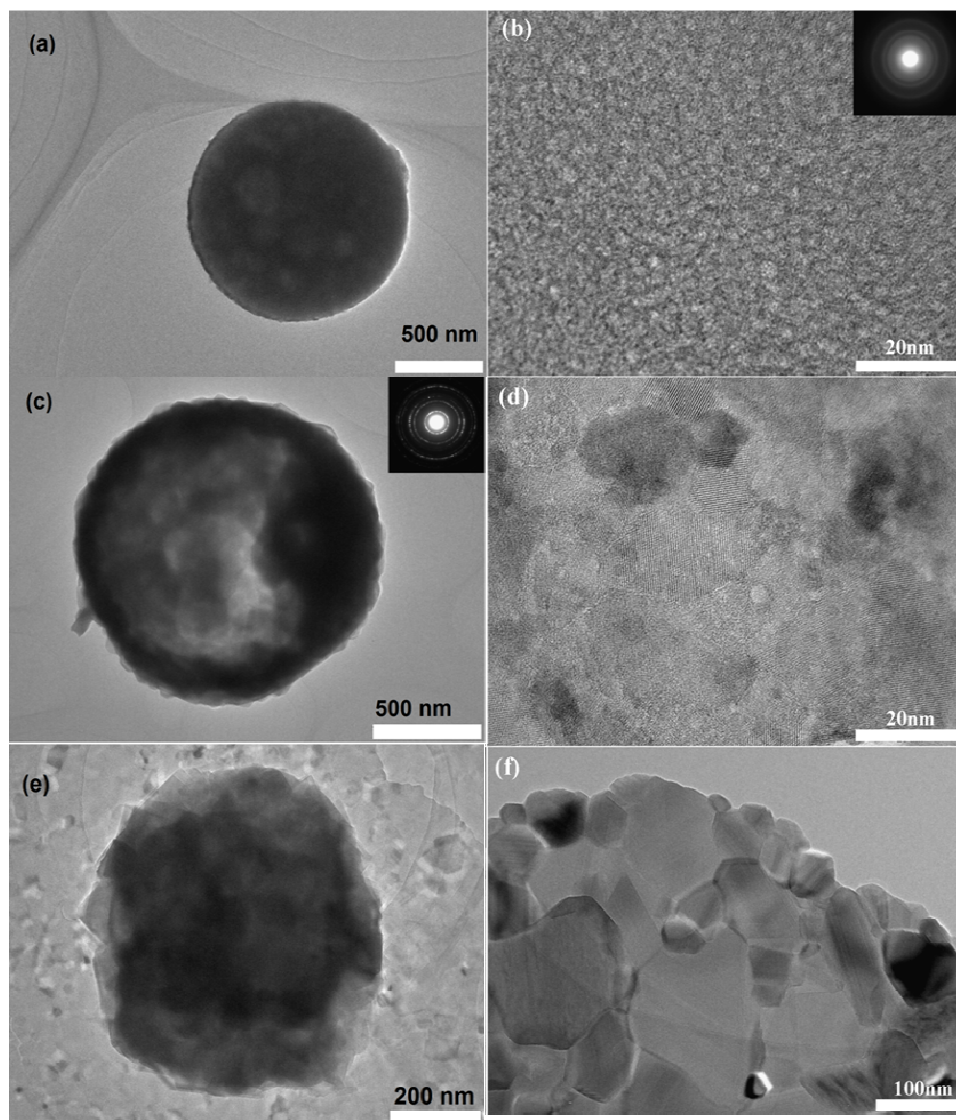


Figure 1. TEM images: (a) raw LTO and (b) a high-resolution image with the inset showing the corresponding selected area electron diffraction (SAED) pattern; (c) LTO-N, with the inset showing the SAED pattern, and (d) a high resolution image; (e) LTO-A, and (f) a high resolution image.

The high resolution TEM images of LTO-N show amorphous features in some areas, which indicate the presence of carbon produced by the decomposition of the organic precursor salts under the final heat treatment in inert atmosphere. To verify

the existence of residual carbon, Raman and energy dispersive X-ray spectroscopy (EDS) were conducted and are shown in **Figure 2**. The Raman spectra of the LTO-N sample shows two peaks at about 1340 and 1590 cm^{-1} , corresponding to the D and G bands of carbonaceous materials, confirming the presence of carbon. Furthermore, these peaks are absent for the LTO-A sample, suggesting that the residual carbon is removed when annealing takes place in air. The EDS mapping (**Figure S2(b)**) also confirms the existence of an even and uniform distribution of carbon in the LTO-N sample. The EDS spectrum, as shown in the inset in Figure S2(b), clearly shows the carbon peak, and the estimated carbon content from EDS is less than 5 wt%. To determine where the carbon is located in this sample, high resolution TEM was performed (Figure 2(b)). The image shows that the carbon is mainly on the $\text{Li}_4\text{Ti}_5\text{O}_{12}$ grain boundaries, as described in the schematic (Figure 2(c)). Thus, it is believed that the carbon on grain boundaries also acts to inhibit growth of the primary particles for the LTO-N sample, for which the TEM images indicate smaller crystal sizes relative to the LTO-A sample. Thermogravimetric analysis (TGA) was also conducted in air to confirm the content of carbon in the samples, as shown in Supplementary Fig. S3. For the LTO-A sample, no obvious weight change can be observed from 100 °C to 750 °C, while there is a weight loss before 440°C and a weight increase in the 440-600 °C range for the LTO-N sample. The weight increase probably relates to the oxidation of Ti^{3+} , which is generated by the reductive atmosphere during the post-annealing process. The presence of Ti^{3+} could be confirmed by XRD refinement and x-ray photoelectron spectroscopy (XPS) measurements, which will be discussed

later. The weight loss is mainly contributed by the carbon burn-off. The weight loss may be counteracted by the weight gain (although it is hard to detect the exact content of Ti^{3+} in the LTO-N) in a particular temperature range, which makes it difficult to determine the precise carbon content in the LTO-N sample from the TGA curve.

Carbon coating or addition has been a traditional way to improve the conductivity of electrode materials, and it is very common to use extra carbon sources (such as citric acid, pitch, polyaniline, or organic ionic liquid [10]) for carbon addition. In this work, we use $\text{Ti}(\text{OCH}_2\text{CH}_2\text{CH}_2\text{CH}_3)_4$ and CH_3COOLi as starting materials, with the $-(\text{OCH}_2\text{CH}_2\text{CH}_2\text{CH}_3)_4$ and $-\text{COOCH}_3$ groups acting as atomic level carbon sources. In this way, we can achieve uniform carbon distribution, and the carbon is located along the grain boundaries. It is highly likely that the affinity created between carbon and $\text{Li}_4\text{Ti}_5\text{O}_{12}$ during the synthetic procedures would be better than post-synthetic carbon coating through the use of additional carbon sources. As shown in Figure 2(c), the LTO-N nanoparticles are agglomerated with a thin layer of carbon between them, and such a well-formed carbon- $\text{Li}_4\text{Ti}_5\text{O}_{12}$ network will effectively facilitate both electron and lithium ion transportation in the material. This would therefore significantly improve the electrochemical performance of the electrodes.

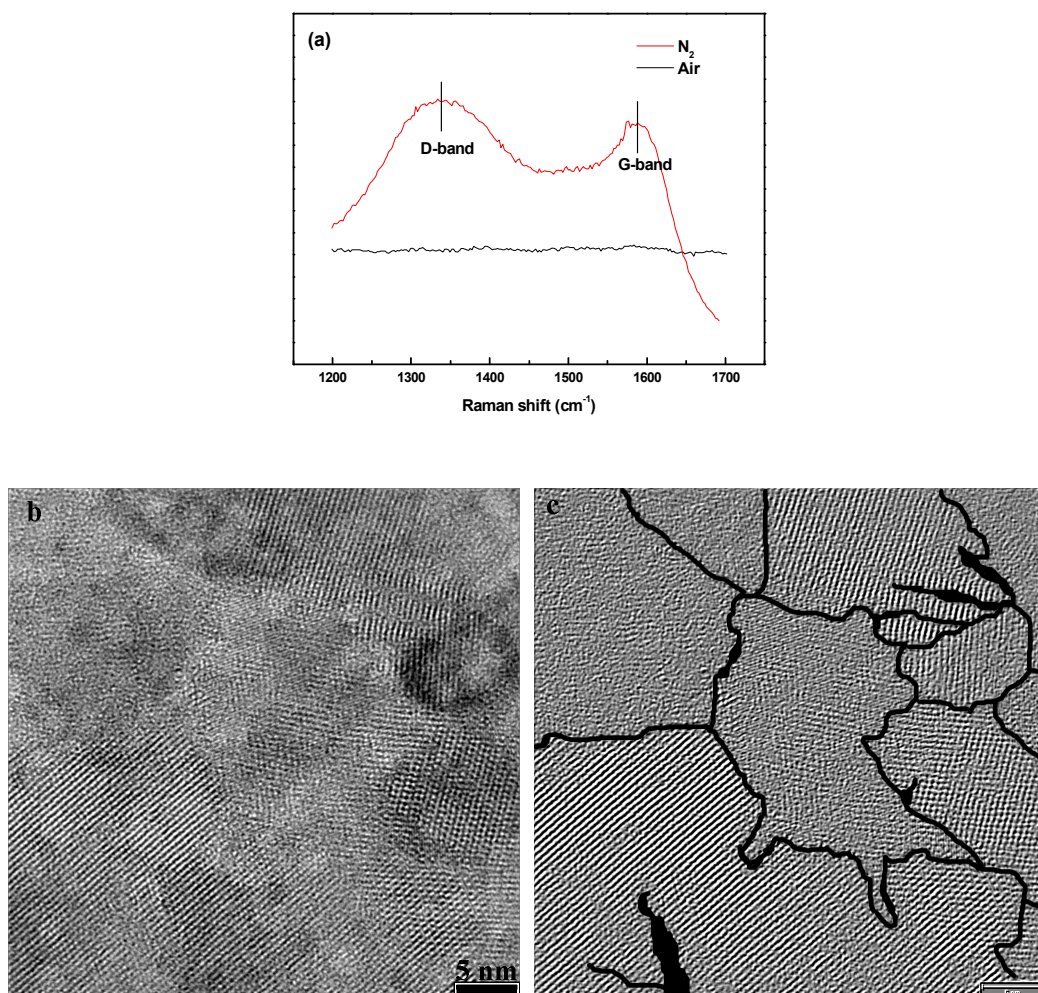


Figure 2. (a) Raman spectra of LTO samples annealed in N₂ and air, respectively; (b) high resolution TEM image of the LTO-N sample; and (c) schematic diagram of carbon distribution on grain boundaries.

For LTO-N, the heat treatment atmosphere was slightly reductive, which presumably reduced tetravalent Ti in Li₄Ti₅O₁₂ to trivalent Ti to some extent. Jung et al. [10] recently reported a change in Ti valence in carbon-coated Li₄Ti₅O₁₂ samples annealed in argon. Thus, to determine the Ti valence, X-ray photoelectron spectroscopy was conducted on our spray pyrolyzed LTO-N sample, and the results are shown as Fig. S4. The sample was stored in ambient atmosphere, and the outer

surface is composed of tetravalent Ti (Fig. S4(a)). The two peaks located at 458.5 and 464.1 eV can be assigned to the core level of $\text{Ti}^{4+} 2p_{3/2}$ and $\text{Ti}^{4+} 2p_{1/2}$, respectively. However, after Ar ion etching, two additional peaks located at 456.5 and 461.8 eV ascribed to $\text{Ti}^{3+} 2p_{3/2}$ and $\text{Ti}^{3+} 2p_{1/2}$, respectively, could be identified, suggesting the presence of Ti^{3+} species [10].

Rietveld refinement of $\text{Li}_4\text{Ti}_5\text{O}_{12}$ models with XRD data (shown as **Figure 3** and details presented in **Table S1**) illustrates a larger lattice parameter for LTO annealed in N_2 ($a = 8.3692(3) \text{ \AA}$) compared to LTO annealed in air ($a = 8.3607(1) \text{ \AA}$). The lattice parameter is expected to increase if some Ti^{4+} is transformed to Ti^{3+} , because of the larger ionic radius of Ti^{3+} (0.67 \AA) compared to Ti^{4+} (0.605 \AA) [12]. Digital photographs of the two powder samples are also shown as insets in Figure 3, and clearly, the sample annealed in air is white, while the sample annealed in N_2 is grey. The color change from white to grey may not be entirely due to the presence of carbon, but also due to the partial formation of Ti^{3+} [10]. The difference in crystallite sizes between LTO-N and LTO-A can be clearly seen in the peak shapes of the XRD data, with LTO-N featuring broader peaks characteristic of smaller crystallites, relative to LTO-A with sharper peaks characteristic of larger crystallites. If we consider particle size as the major contributor to the broadening of peak shapes and use peak-profile functions (particle-size broadening effect) in Rietveld analysis to investigate average crystallite sizes, we find that the average crystallite sizes follow $\text{LTO-A} > \text{LTO-N}$ and that the ratio of average crystallite sizes, $\text{LTO-A} : \text{LTO-N}$, is 2:1, that is, the average crystallite size for the LTO-N is half the size of the average

crystallite of LTO-A, which is consistent with the TEM results shown in Figure 1.

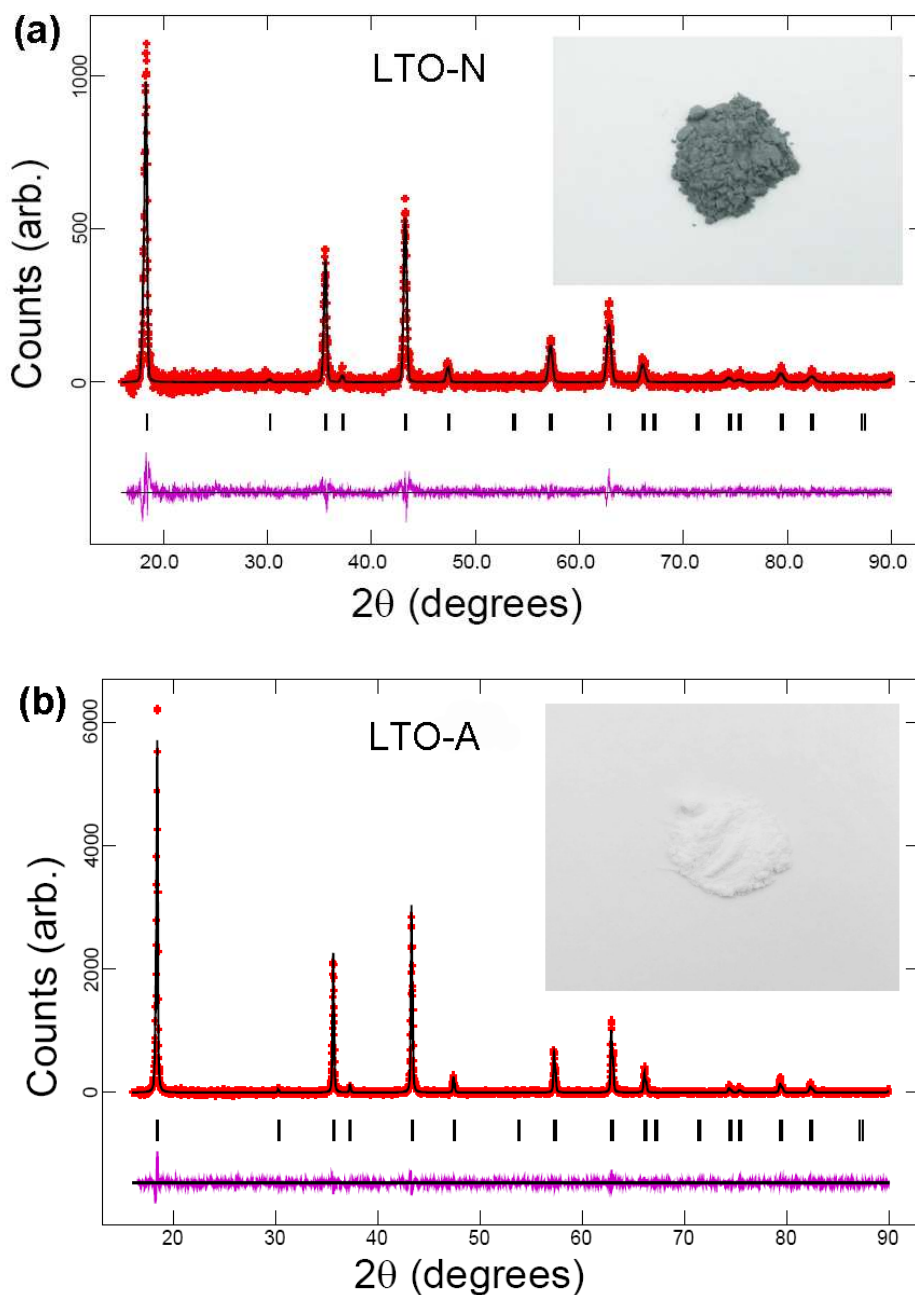


Figure 3. Rietveld refinements of the $\text{Li}_4\text{Ti}_5\text{O}_{12}$ structural model based on XRD data for LTO-N (a) and LTO-A (b). Crosses (×) indicate the collected data, the solid line through the data is the calculated model, the purple line below is the difference between observed and calculated, and the vertical lines indicate Bragg reflections. The insets contain digital photographs of the powder samples, respectively.

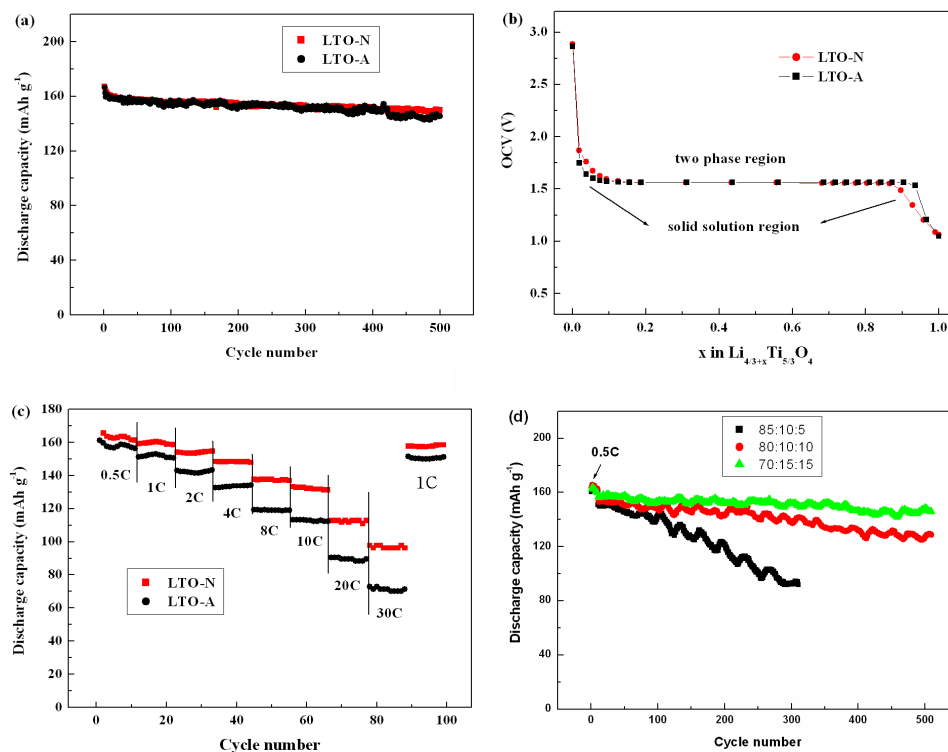


Figure 4. Electrochemical performance: (a) cyclability of LTO-N and LTO-A at 0.5 C, (b) open circuit potential of LTO-N and LTO-A samples, (c) rate capability of LTO-N and LTO-A samples from 0.5 C to 30 C (with charge and discharge process at the same C-rate), (d) cyclability of LTO samples at 10 C with different ratios of active material: carbon black: binder (with the charge rate fixed at 1 C = 175 mA g⁻¹).

Figure 4(a) compares the cycling performances of both annealed samples at a current rate of 0.5 C (87.5 mA g⁻¹). The initial reversible capacities are 165 mAh g⁻¹ and 162 mAh g⁻¹, respectively, for LTO-N and LTO-A, and both show good capacity retention of 90.9% and 89.5%, respectively, up to 500 cycles. The open circuit potentials for both samples versus their lithium composition are displayed in Fig. 4(b). The open circuit voltage (OCV) curves are sloping at the beginning and at the end of

the Li insertion process, with a flat voltage plateau in between. The slope indicates single phase (solid solution) regions in the discharge process corresponding to $\text{Li}_{4+\delta}\text{Ti}_5\text{O}_{12}$ (beginning) and $\text{Li}_{7-\gamma}\text{Ti}_5\text{O}_{12}$ (end), and the flat part corresponds to a two-phase reaction between the two end members, where both δ and γ are small [13]. The LTO-N sample clearly shows an increase in the solid solution region by having a longer slope relative to the LTO-A sample. It is proposed that the two phase solubility could be related to particle size, strain, interface and surface energy contributions, etc. [14]. In the present study, it might be attributed to the smaller crystallite sizes and possible presence of Ti^{3+} in the LTO-N sample. Wang et al. [10] reported that the single phase reaction shows a significantly higher lithium diffusion coefficient than the two-phase reaction region, and therefore, a sample with a larger single phase region should show favorable high rate performance.

Rate capabilities of LTO-N and LTO-A samples from 0.5 C to 30 C are shown in Figure 4(c). Both samples show stable cycling performance at each applied current density, but LTO-N shows a higher discharge capacity than LTO-A, especially at high rates. LTO-N exhibits discharge capacities of 160 mAh g^{-1} , 148 mAh g^{-1} , 132 mAh g^{-1} , and 112 mAh g^{-1} for 1 C (175 mA g^{-1}), 4 C (0.7 A g^{-1}), 10 C (1.75 A g^{-1}), and 20 C (3.5 A g^{-1}), respectively, and a discharge capacity of 96 mAh g^{-1} is also achieved at 30 C (5.25 A g^{-1}). Moreover, the discharge capacity increases to 157 mAh g^{-1} when the discharge rate returns back to 1 C. The corresponding galvanostatic charge-discharge curves at different C-rates are shown in **Figure S5**. This figure shows that the difference between the charge and discharge voltage plateaus tend to increase with

increasing current density. The outstanding rate capability of the LTO-N sample can be attributed to the following factors: (i) carbon located on grain boundaries, enhancing the conductivity; (ii) carbon inhibiting crystal growth during annealing, resulting in nanoparticles which feature the shorter lithium diffusion lengths that are favorable for high rate performance; and (iii) the possible presence of Ti^{3+} in LTO-N, which enhances electronic conductivity and thus improves performance. The conductivity enhancement with Ti^{3+} is due to the presence of one extra electron in trivalent Ti compared to tetravalent Ti, which exhibits the insulating properties arising from empty Ti 3d states [15].

It is well known that higher carbon content is favorable for high rate performance in laboratory coin cells [16]. Thus, the cycling performance of LTO-N electrodes with different weight ratios of active material, carbon black, and binder were investigated. Weight ratios of active material : carbon : polyvinylidene difluoride (PVDF) binder of 85:10:5, 80:10:10, and 70:15:15 were investigated, and the cycling stabilities at 10 C after 0.5 C activation for the first 10 cycles are shown in Figure 4(d). The capacity of the electrode with a ratio of 85:10:5 evidently decreases after 100 cycles, while the cell with a ratio of 80:10:10 shows moderate cycling capacity retention. The 70:15:15 ratio shows the best retention, exhibiting a discharge capacity of 145.8 mAh g^{-1} up to 500 cycles, with capacity retention of 92.9% relative to the initial cycle at 10 C (156.9 mA g^{-1}).

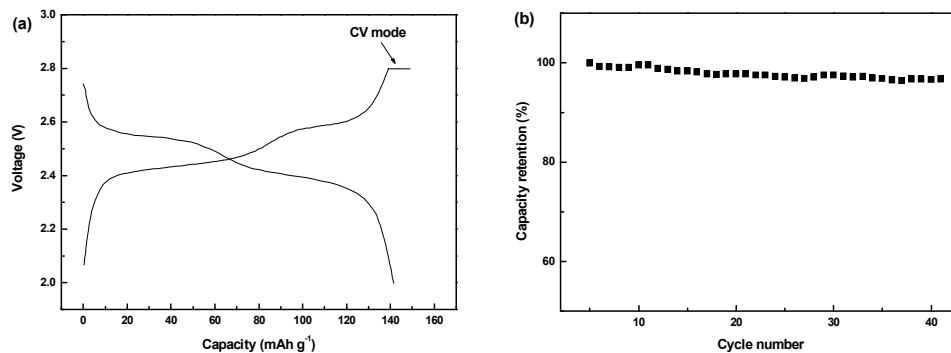


Figure 5. $\text{Li}_4\text{Ti}_5\text{O}_{12}$ anode and $\text{Li}(\text{Co}_{0.16}\text{Mn}_{1.84})\text{O}_4$ cathode full battery tests: (a) galvanostatic charge/discharge curves for the first cycle, and (b) cycling performance.

A full battery test was also undertaken using $\text{Li}(\text{Co}_{0.16}\text{Mn}_{1.84})\text{O}_4$ (LCMO) as the cathode and LTO-N as the anode. The voltage vs. capacity curves of the LCMO half cell are shown in **Figure S6**. Two discharge voltage plateaus are exhibited at about 4.1 and 4.0 V vs. Li^+/Li . The discharge capacities of the cathode material are 103 and 99 mAh g^{-1} when cycled at the current densities of 87.5 (0.5 C for $\text{Li}_4\text{Ti}_5\text{O}_{12}$) and 175 mA g^{-1} (1 C for $\text{Li}_4\text{Ti}_5\text{O}_{12}$), respectively. The weight ratio of the LTO-N electrode to the LCMO electrode in the full battery was designed such that the electrode capacity ratio is 1:1. The testing conditions employed involved a constant current charge step at the rate of 0.5 C, followed by a constant voltage (CV) step until the current decreased to 0.01 C. The discharge process was at the rate of 1 C (1 C = 175 mA g^{-1}), except for the first three cycles, where activation was performed at a current rate of 0.1 C. **Figure 5(a)** shows the galvanostatic charge/discharge curves, with discharge cell voltage plateaus of about 2.5 and 2.4 V and a discharge capacity of 140 mAh g^{-1} (calculated based on $\text{Li}_4\text{Ti}_5\text{O}_{12}$). Note that the capacity of the constant voltage charge mode only accounts for about 2.5% of the whole charge capacity. Due to the various

engineering factors, such as electrode fabrication, geometric effects, and load balancing with two distinctly different single electrodes integrated via a laboratory scale fabrication procedure into a full cell, the electrochemical performance of the $\text{Li}_4\text{Ti}_5\text{O}_{12}$ electrode in the full battery is not as good as that in a half cell. Nonetheless, the full battery exhibits good capacity retention, as shown in **Figure 5(b)**. The capacity at the 40th cycle retains 96.8% of the discharge capacity for the first cycle.

Conclusion

We report a promising high rate long cycle life anode candidate based on $\text{Li}_4\text{Ti}_5\text{O}_{12}$ for high power lithium ion battery applications, which is synthesized by the spray pyrolysis technique and is highly feasible for industrial use. Spray pyrolyzed $\text{Li}_4\text{Ti}_5\text{O}_{12}$ annealed in N_2 for short periods of time features carbon on the grain boundaries, which originates from the decomposition of the organic synthetic precursors. The reductive atmosphere during carbon formation simultaneously introduces Ti^{3+} into the sample. The in-situ incorporation of carbon and Ti^{3+} not only improves the electric conductivity of the material, but also inhibits the growth of $\text{Li}_4\text{Ti}_5\text{O}_{12}$ crystals, which are favorable for electrochemical performance. The as-prepared $\text{Li}_4\text{Ti}_5\text{O}_{12}$ exhibited outstanding electrochemical behavior, even at a high C-rate. Moreover, in full battery tests, the material also shows excellent performance, demonstrating its applicability as a good anode candidate for lithium ion batteries.

Experimental

Synthesis: The clear transparent precursor solution was prepared by dissolving a stoichiometric ratio of lithium acetate and titanium butoxide in ethanol to obtain a 0.5

M solution. The solution was sprayed into the pyrolysis furnace at a temperature of 800 °C using two fluids spray nozzle and air as a carrier gas at a flow rate of 6.5 mL min⁻¹ to obtain raw Li₄Ti₅O₁₂ (designated as raw LTO). Then, the raw LTO sample was post-annealed in N₂ (designated as LTO-N) and air (designated as LTO-A) at 800 °C for 1 h with a ramping speed of 5° min⁻¹.

Characterization: TEM images were collected with a JEOL 2011F instrument. XRD data were collected on a PANalytical X'Pert Pro diffractometer with Cu K α radiation. Rietveld refinements were carried out using the GSAS [17] suite of programs with the EXPGUI [18] interface. Raman spectroscopy was performed on a Jobin Yvon HR800. EDS spectra were collected with a JEOL JSM-6460A instrument. XPS was conducted using Al K α radiation at 12 kV. The electrochemical tests were carried out via CR2032 coin type cells. Typically, the working electrodes were prepared by mixing the as-prepared Li₄Ti₅O₁₂ samples, carbon black, and polyvinylidene difluoride (PVDF) at a weight ratio of 85:10:5 and pasting onto Cu foil. The coated electrodes were dried in a vacuum oven at 110 °C for 8 h. The active material loading quantity was about 2 mg cm⁻¹. Coin cells were assembled in an argon-filled glove box (Mbraun, Unilab, Germany) by stacking a porous polypropylene separator containing liquid electrolyte between the composite electrode and a lithium foil counter electrode. The electrolyte consisted of a solution of 1 M LiPF₆ in ethylene carbonate (EC)/ dimethyl carbonate (DMC) (1:1, in volume). The discharge/charge measurements were conducted on a Land CT2001A tester. For the full battery tests, Li(Co_{0.16}Mn_{1.84})O₄ (LCMO) was used as the cathode and synthesized as reported previously [19]. The composition of the

electrode is 80:10:10 by weight (LCMO : carbon black : PVDF) and pasted onto Al foil.

Acknowledgements

Financial support provided by the Australian Research Council (ARC) through ARC Discovery Projects DP1094261 and DP1093952 is gratefully acknowledged. The authors would like to thank Dr. Tania Silver at the University of Wollongong for critical reading of the manuscript. We also acknowledge Dr. Darren Attard and Dr. Ivan Nevirkovets for SEM, Raman, and XPS measurements.

References

- [1] M. Armand, J. M. Tarascon, *Nature* **2008**, *451*, 652.
- [2] P. G. Bruce, B. Scrosati, J. M. Tarascon, *Angew. Chem. Int. Ed.* **2008**, *47*, 2930.
- [3] J. B. Goodenough, Y. Kim, *Chem. Mater.* **2010**, *22*, 587.
- [4] S. S. Zhang, K. Xu, T. R. Jow, *J. Power Sources* **2006**, *160*, 1349.
- [5] a) K. Amine, I. Belharouak, Z. H. Chen, T. Tran, H. Yumoto, N. Ota, S.-T. Myung, Y.-K. Sun, *Adv. Mater.* **2010**, *22*, 3052; b) A. S. Prakash, P. Manikandan, K. Ramesha, M. Sathiya, J. M. Tarascon, A. K. Shukla, *Chem. Mater.* **2010**, *22*, 2857. c) J. Liu, K. Song, P.A. Aken, J. maier, Y. Yu, *Nano Letters* **2014**, *14*, 2597. d) B. Wan, J. Wang, J. Cao, H. Ge, Y. Tang, *J. Power Sources* **2014**, *266*, 150.
- [6] a) K. Zaghib, M. Simoneau, M. Armand, M. Gauthier, *J. Power Sources* **1999**,

- 81-82, 300; b) Z. Yang, D. Choi, S. Kerisit, K. M. Rosso, D. Wang, J. Zhang, G. Graff, J. Liu, *J. Power Sources* **2009**, *192*, 588.
- [7] a) K. M. Colbow, J. R. Dahn, R. R. Haering, *J. Power Sources* **1989**, *26*, 397; b) E. Ferg, R. J. Gummow, A. Dekock, M. M. Thackeray, *J. Electrochem. Soc.* **1994**, *141*, L147; c) T. Ohzuku, A. Ueda, N. Yamamoto, *J. Electrochem. Soc.* **1995**, *142*, 1431.
- [8] a) C. H. Chen, J. T. Vaughey, A. N. Jansen, D. W. Dees, A. J. Kahaian, T. Goacher, M. M. Thackeray, *J. Electrochem. Soc.* **2001**, *148*, A102; b) C. Y. Ouyang, Z. Y. Zhong, M. S. Lei, *Electrochem. Commun.* **2007**, *9*, 1107; c) M. Wagemaker, E. R. H. van Eck, A. P. M. Kentgens, F. M. Mulder, *J. Phys. Chem. B* **2009**, *113*, 224.
- [9] a) L. Cheng, J. Yan, G. N. Zhu, J. Y. Luo, C. X. Wang, Y. Y. Xia, *J. Mater. Chem.* **2010**, *20*, 595; b) W. J. H. Borghols, M. Wagemaker, U. Lafont, E. M. Kelder, F. M. Mulder, *J. Am. Chem. Soc.* **2009**, *131*, 17786.
- [10] a) H. G. Jung, S.-T. Myung, C. S. Yoon, S.-B. Son, K. H. Oh, K. Amine, B. Scrosati, Y.-K. Sun, *Energy Environ. Sci.* **2011**, *4*, 1345; b) L. Zhao, Y. S. Hu, H. Li, Z. X. Wang, L. Q. Chen, *Adv. Mater.* **2011**, *23*, 1385; c) Y. G. Wang, H. M. Liu, K. X. Wang, H. Eiji, Y. R. Wang and H. S. Zhou, *J. Mater. Chem.* **2009**, *19*, 6789; d) M. M. Rahman, J. Z. Wang, M. F. Hassan, D. Wexler, H. K. Liu, *Adv. Energy. Mater.* **2011**, *1*, 212; e) L. Cheng, X. L. Li, H. J. Liu, H. M. Xiong, P. W. Zhang, Y. Y. Xia, *J. Electrochem. Soc.* **2007**, *154*, A692.
- [11] a) K. Konstantinov, S. Bewlay, G. X. Wang, M. Lindsay, J. Z. Wang, H. K. Liu, S. X. Dou, J. H. Ahn, *Electrochim. Acta* **2004**, *50*, 421; b) J. Liu, T. E. Conry, X. Y.

- Song, M. M. Doeff, T. J. Richardson, *Energy Environ. Sci.* **2011**, *4*, 885; c) M. R. Yang, T. H. Teng, S. H. Wu, *J. Power Sources* **2006**, *159*, 307; d) B. Wang, K. Konstantinov, D. Wexler, H. Liu, G. X. Wang, *Electrochim. Acta* **2009**, *5*, 1420; e) S. H. Ng, J. Wang, D. Wexler, K. Konstantinov, Z. P. Guo, H. K. Liu, *Angew. Chem. Int. Ed.* **2006**, *45*, 6896.
- [12] R. D. Shannon, *Acta Crystallogr. Sect. A: Cryst. Phys. Diffr. Theor. Gen. Crystallogr.* **1976**, *32*, 751.
- [13] M. Wagemaker, D. R. Simon, E. M. Kelder, J. Schoonman, C. Ringpfeil, U. Haake, D. Lützenkirchen-Hecht, R. Frahm, F. M. Mulder, *Adv. Mater.* **2006**, *18*, 3169.
- [14] a) N. Meethong, H. Y. S. Huang, W. C. Carter, Y. M. Chiang, *Electrochem. Solid State Lett.* **2007**, *10*, A134; b) G. Kobayashi, S. Nishimura, M. S. Park, R. Kanno, M. Yashima, T. Ida, A. Yamada, *Adv. Funct. Mater.* **2009**, *19*, 395; c) N. Meethong, H. Y. S. Huang, S. A. Speakman, W. C. Carter, Y. M. Chiang, *Adv. Funct. Mater.* **2007**, *17*, 1115; d) M. Wagemaker, F. M. Mulder, A. Van der Ven, *Adv. Mater.* **2009**, *21*, 2703.
- [15] a) K. S. Park, A. Benayad, D. J. Kang, S. G. Doo, *J. Am. Chem. Soc.* **2008**, *130*, 14930; b) J. Wolfenstine, U. Lee, J. L. Allen, *J. Power Sources* **2006**, *154*, 287.
- [16] a) B. Kang, G. Ceder, *Nature* **2009**, *458*, 190; b) T. Beuvier, M. Richard-Plouet, M. M. Granvalet, T. Brousse, O. Crosnier, L. Brohan, *Inorg. Chem.* **2010**, *49*, 8457.
- [17] A. C. Larson, R. B. Von Dreele, *General Structure Analysis System (GSAS)*, Los

Alamos National Laboratory Report LAUR **1994**, 86-748.

[18] B. H. Toby, *J. Appl. Cryst.* **2001**, *34*, 210.

[19] M. V. Reddy, G. V. S. Rao, B. V. R, Chowdari, *J. Phys. Chem. C* **2007**, *111*, 11712.

The table of contents entry

Nanocrystalline $\text{Li}_4\text{Ti}_5\text{O}_{12}$ was synthesized by an in-situ spray pyrolysis technique followed by heat treatment in N_2 for short periods of time, resulting in self-contained carbon originating from the organic synthetic precursors. The excellent high rate capability and full battery tests indicate that this is a promising anode candidate for high power lithium-ion batteries.

Keywords

$\text{Li}_4\text{Ti}_5\text{O}_{12}$, spray pyrolysis, anode, high rate, lithium ion batteries

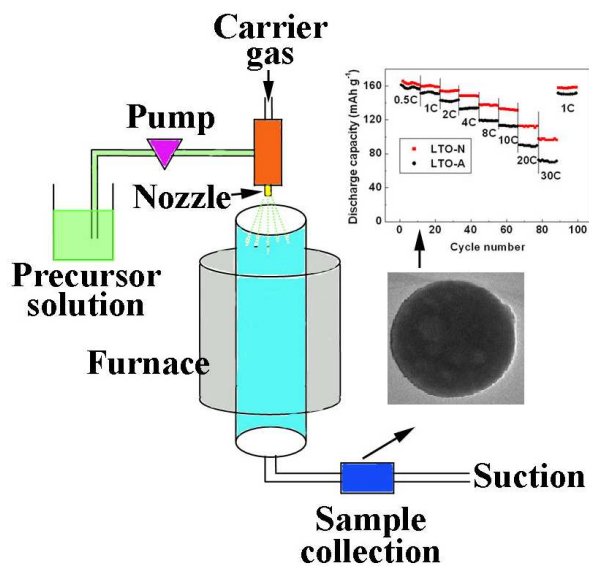
Authors

Guodong Du, Brad R. Winton, Israa M. Hashim, Neeraj Sharma, Konstantin Konstantinov, M. V. Reddy, Zaiping Guo**

Title

Mass production of $\text{Li}_4\text{Ti}_5\text{O}_{12}$ with conductive network via In-situ spray pyrolysis as a long cycle life, high rate anode material for lithium ion batteries

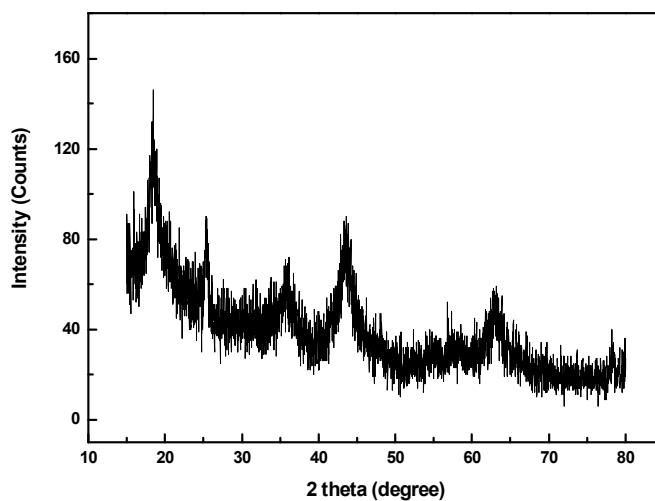
TOC Figure



Supporting Information

Mass production of $\text{Li}_4\text{Ti}_5\text{O}_{12}$ with conductive network via In-situ spray pyrolysis as a long cycle life, high rate anode material for lithium ion batteries

Guodong Du, Brad R. Winton, Israa M. Hashim, Neeraj Sharma, Konstantin Konstantinov, M. V. Reddy, Zaiping Guo**



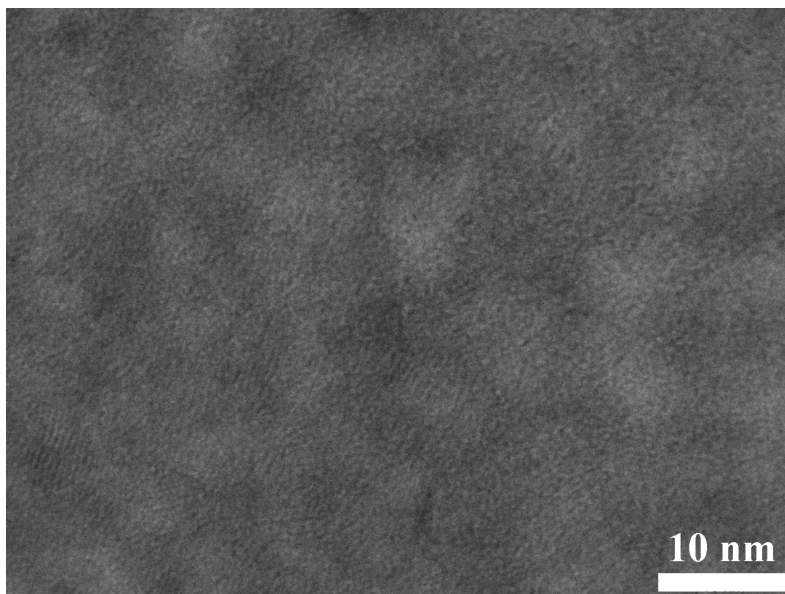


Figure S1. (a) XRD pattern and (b) high resolution TEM image of the raw $\text{Li}_4\text{Ti}_5\text{O}_{12}$.

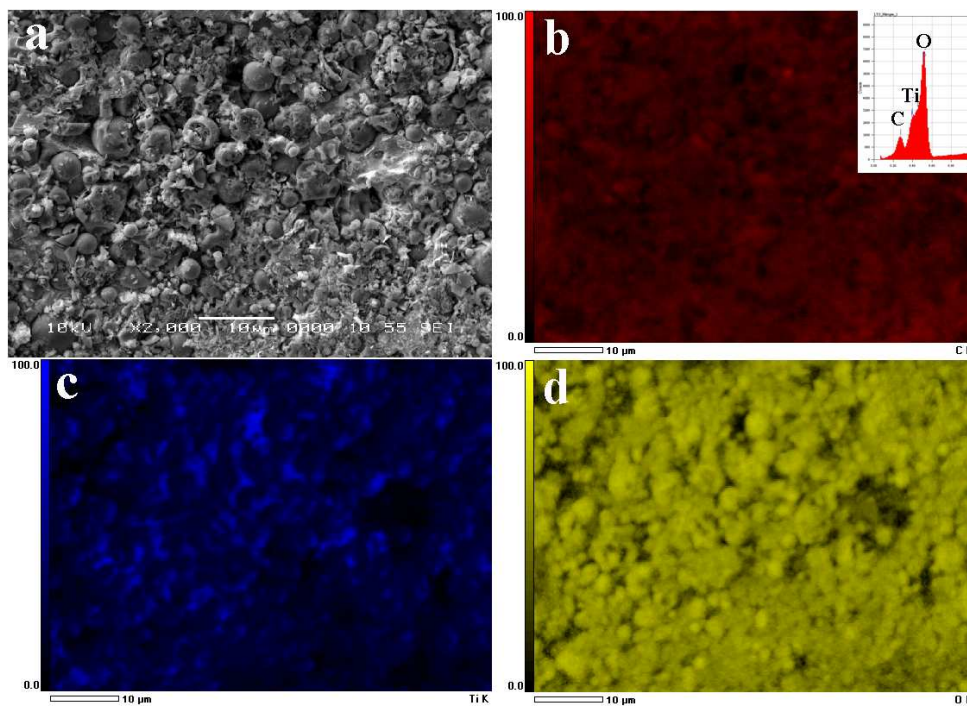


Figure S2. EDS mapping of sample LTO-N: (a) SEM image, (b) carbon distribution, with the inset showing the EDS spectrum, (c) titanium distribution, (d) oxygen distribution.

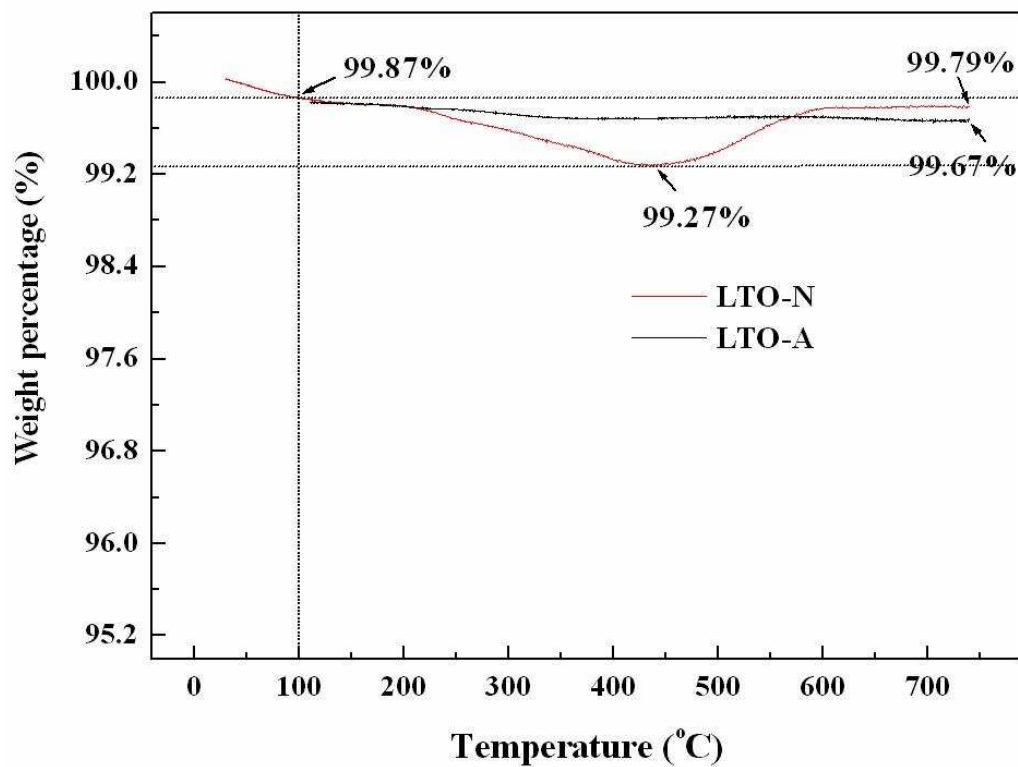


Figure S3. The TGA curves of LTO-N and LTO-A samples.

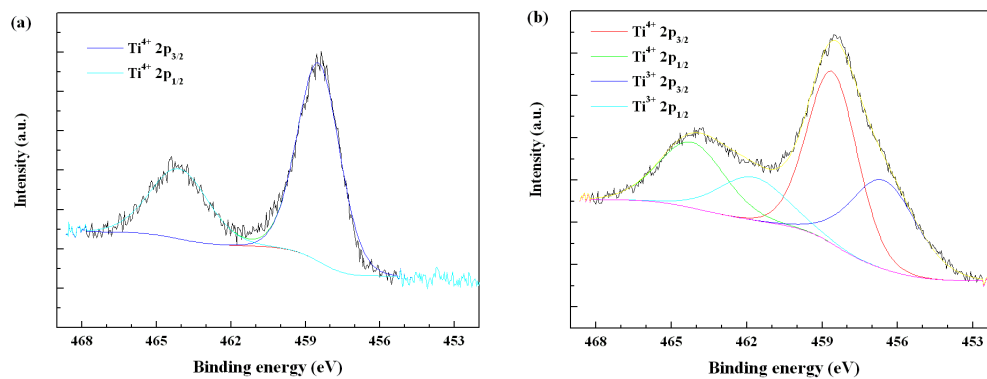


Figure S4. X-ray photoelectron Ti 2p core level spectra of the LTO-N sample: (a) outer surface layer and (b) after Ar ion etching.

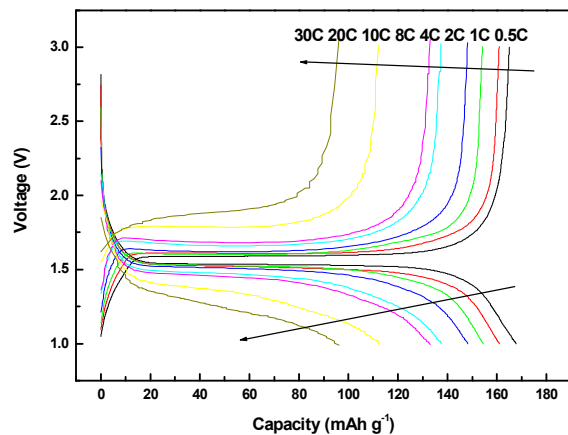


Figure S5. Galvanostatic charge/discharge curves of $\text{Li}_4\text{Ti}_5\text{O}_{12}$ annealed in N_2 at different C-rates.

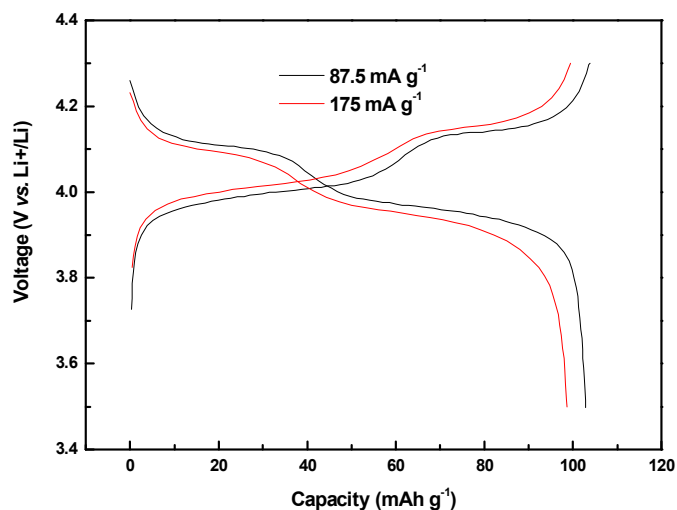


Figure S6. Galvanostatic charge/discharge curves of $\text{Li}(\text{Co}_{0.16}\text{Mn}_{1.84})\text{O}_4$ vs. Li^+/Li at current densities of 87.5 mA g^{-1} and 175 mA g^{-1} .

Table S1. Lattice parameter, oxygen positional parameter (only atomic parameter that was refined), atomic displacement parameters and the fitting statistics for the Rietveld refinements.

Sample	Lattice Parameter (Å)	Oxygen positional parameter $x = y = z$	Atomic displacement parameters ($100 \cdot U_{\text{iso}}$)	Rp	wRp	χ^2 (goodness-of-fit term)

			Li, Li/Ti, O			
N ₂	8.3692(3)	0.2628(2)	4.9(6), 3.9(1), 3.0(1)	8.87	11.38	1.33
Air	8.3607(1)	0.2633(2)	6.8(8), 4.1(1), 3.2(1)	7.19	9.25	1.61